Black Holes in the MMA–DMF Framework: Resolving the Information and Entropy Paradoxes

Paulo Adriano

Abstract

The MMA–DMF framework modifies gravity by adding a single geometric scalar degree of freedom with a characteristic energy scale of order 100 TeV. In this work we assemble the black–hole sector of MMA–DMF and show how it leads to a concrete, testable resolution of both the entropy and information paradoxes. Starting from a static, spherically symmetric regular metric with a de Sitter core, we derive the thermodynamic quantities of MMA–DMF black holes, including a corrected entropy $S_{MMA--DMF}(A)$, a modified evaporation law with a finite remnant mass, and a self–consistent Page curve in which the black–hole entropy decreases while the radiation entropy increases, saturates and eventually falls. We then systematise all strong–gravity and information tests present in the documentation: neutron–star and Super–TOV configurations that fix the high–density scalar stiffness; tests of intermediate–mass and microscopic black holes; a "Sad Trombone" fast–radio–burst test which constrains scalar relaxation and feeds into microscopic evaporation; ringdown tests (including scalar breathing modes and quasinormal–mode deviations), shadow and photon–ring tests, and modified ISCO spectra that reveal spin–scalar–charge degeneracies. Dedicated information–paradox tests quantify the deviation of MMA–DMF quasinormal modes from Kerr, the structure of gravitational–wave echoes, and the Total Determinism Test for Black Holes (TDT–BH), which relates the corrected entropy, echo delays and quasinormal–mode shifts across the full mass spectrum from microscopic remnants to supermassive objects. Using these ingredients we demonstrate that MMA–DMF black holes are free of curvature singularities, possess a finite and computable entropy at all stages of their evolution, obey a generalised second law and can preserve quantum information through a combination of regular cores, long–lived remnants and delayed echo channels. At the same time, the model predicts specific observational signatures—in particular, millisecond–scale echoes in stellar–mass mergers, percent–level deviations in higher–order quasinormal modes and degeneracies between spin and scalar charge in accretion spectra—which render its proposed resolution of the information and entropy paradoxes empirically falsifiable.

1 Introduction

General Relativity (GR) has passed every experimental test in weak and moderately strong gravitational fields, from the perihelion of Mercury to binary pulsars and gravitational–wave detections. Yet, when extrapolated to its natural ultraviolet and infrared limits, the theory encounters three conceptual and phenomenological problems. First, its classical solutions contain curvature singularities at the Big Bang and at the centres of black holes, where the mathematical description breaks down and no well–posed Cauchy evolution exists. Second, GR is formulated as a purely geometric theory on a differentiable manifold and remains difficult to reconcile with the quantum description of matter. Third, the concordance cosmological model based on GR, cold dark matter and a cosmological constant requires two dark components which have not been detected microscopically, and exhibits statistically significant tensions in key observables such as the Hubble constant and the amplitude of matter clustering.

The MMA–DMF framework addresses these issues by promoting the gravitational sector to include a single geometric scalar degree of freedom ϕ with a fundamental energy scale

$M \simeq 100\,\mathrm{TeV}$. Rather than postulating a separate dark matter fluid and a dark energy component, MMA–DMF replaces the "hypothesis of matter" by a "hypothesis of gravity": the scalar couples non–minimally to curvature invariants and to the trace of the energy–momentum tensor, modifying the infrared and ultraviolet behaviour of gravity while reproducing GR in the intermediate regime relevant for most current tests. At low curvatures and densities the scalar is light and mediates long–range effects that mimic dark matter and dark energy. At high curvature and density it becomes heavy through a curvature–dependent effective mass, implementing a mechanism of *geometric locking* which regularises would–be singularities.

Previous work on MMA–DMF has focused mainly on cosmological and galactic scales, where the scalar explains late–time acceleration, alleviates the Hubble and S_8 tensions and reproduces galaxy rotation curves and cluster dynamics without particle dark matter. The same microphysics, however, has nontrivial consequences in the strong–field regime. The effective mass

$$m_{\rm eff}^2(\rho, \mathcal{G}) \simeq \frac{\rho}{M^2} - \mu_{\rm bare}^2 + \frac{\beta_{\rm GB}}{2M^2}\,\mathcal{G}, \tag{1}$$

depends both on the matter density ρ and on the Gauss–Bonnet invariant $\mathcal{G}$, with $\beta_{\rm GB}$ a dimensionless coupling. In the vicinity of classical singularities, $\mathcal{G}$ grows rapidly and drives $m_{\rm eff}$ to large positive values, dynamically freezing ϕ near a symmetric vacuum and preventing curvature blow–up. In cosmology this mechanism converts the Big Bang into a nonsingular bounce. In compact objects it regularises the interior of neutron stars and black holes, replacing singular cores by finite–density de Sitter–like regions.

In the black–hole sector, the static spherically symmetric solution of MMA–DMF takes the form of a modified Hayward–de Sitter geometry,

$$ds^2 = -f(r)\,dt^2 + \frac{dr^2}{f(r)} + r^2 d\Omega^2, \qquad f(r) = 1 - \frac{2GM_{\rm BH}r^2}{r^3 + 2GM_{\rm BH}L^2 + \epsilon L^3}, \tag{2}$$

where $M_{\rm BH}$ is the black–hole mass, $L \sim 1/M \approx 1 \times 10^{-19}\,\mathrm{m}$ is a regularisation length fixed by the fundamental scale and ϵ is an $\mathcal{O}(1)$ core parameter. At large radii $r \gg (2GM_{\rm BH}L^2)^{1/3}$ the metric reduces to Schwarzschild with corrections suppressed by $(L/r)^2$, ensuring compatibility with Solar–System tests and with the external geometry of astrophysical black holes. Near the centre the metric approaches a de Sitter core, curing the curvature singularity of the classical solution and providing a well–defined interior Cauchy problem.

This regular structure affects not only the interior but also dynamical and observational properties of black holes. The modified effective potential for perturbations develops a secondary barrier close to the inner core, creating a resonant cavity between the photon sphere and the reflective region. Gravitational–wave perturbations excited by a binary merger can therefore undergo multiple reflections, generating a train of late–time echoes in addition to the standard ringdown. The same scalar sector stiffens the equation of state of neutron–star matter at supranuclear densities, giving rise to a Super–TOV branch of compact stars which fills the mass gap between ordinary neutron stars and the lightest black holes, and alters the population of intermediate–mass and microscopic black holes.

The existence of a regular core, a high–density scalar sector and a finite curvature scale suggests a natural route towards resolving the black–hole entropy and information paradoxes. In the standard semiclassical picture based on GR, a collapsing star forms a singular black hole whose horizon area encodes an entropy $S_{\rm BH} = A/4G$, while Hawking radiation slowly evaporates the horizon in an apparently thermal state. If the evaporation proceeds to completion, the final radiation state appears mixed even when the initial state is pure, raising a conflict with unitarity. In addition, the entropy stored in the singular region is formally unbounded and ill–defined. In MMA–DMF, by contrast, the interior is nonsingular, black–hole evaporation halts at a finite remnant mass set by M, and the entropy can be corrected and computed consistently at all stages.

The present work assembles and synthesises the entire suite of black–hole and strong–gravity tests developed for MMA–DMF with the explicit goal of addressing the information and entropy paradoxes. The analysis draws on a series of technical reports and audit documents covering: the derivation and validation of the regular black–hole metric; the construction of Super–TOV neutron stars and their application to events like GW190814; tests of intermediate–mass black holes and microscopic remnants; a "Sad Trombone" fast–radio–burst test which constrains scalar relaxation and feeds into microscopic evaporation; a battery of black–hole tests (8.1–8.4) involving scalar breathing modes in ringdown, shadow and photon–ring properties, modified ISCO spectra and spin–scalar–charge degeneracies, and gravitational–wave echoes; and a set of dedicated information–paradox tests which define the corrected entropy, quantify echo delays across the mass spectrum and assemble the Total Determinism Test for Black Holes (TDT–BH).

Our goal is not merely to state that MMA–DMF avoids singularities, but to demonstrate in detail that it admits a consistent thermodynamic description of black holes, with a corrected entropy $S_{MMA--DMF}$, a generalised second law, a unitary Page curve and explicit mechanisms for information retention and release. At the same time, we emphasise that the proposed resolution is not hermetic: it leads to clear observational signatures — millisecond–scale echoes in stellar–mass mergers, small but potentially measurable deviations in higher–order quasinormal modes and degeneracies in accretion spectra — which render the framework falsifiable with current and next–generation observatories.

The remainder of the paper is organised as follows. In Section 2 we summarise the black–hole sector of MMA–DMF, including the scalar effective mass, the regular metric, scalar halos and the high–density equation of state that underpins the Super–TOV branch. Section 3 describes the full test suite and numerical methods, from neutron stars and magnetars to black–hole ringdown, shadows, ISCO spectra and echoes. Section 3.4 focuses on the information and entropy paradox tests, defining the corrected entropy, the evaporation law and the TDT–BH, and presenting the entropy–evolution and Page–curve analysis. Section 4 gathers the quantitative results of all tests and their implications for MMA–DMF parameters. Section 5 discusses how these results fit together into a coherent resolution of the entropy and information paradoxes and what observational signatures are most promising. We conclude in Section 6 with a summary and an outline of future work.

2 The MMA–DMF black hole framework

In this section we summarise the ingredients of the MMA–DMF framework that are directly relevant for black holes and for the information and entropy paradoxes. We start from the effective action and scalar sector, introduce the mechanism of geometric locking which regularises high–curvature regions, present the static regular black–hole metric, and discuss scalar halos, the high–density equation of state and the basic geodesic structure (photon sphere and ISCO).

2.1 Effective action and scalar sector

The gravitational sector of MMA–DMF is formulated in the Einstein frame, where the metric $g_{\mu\nu}$ has the standard Einstein–Hilbert term and a single scalar field ϕ encodes the modifications to gravity. A convenient schematic form of the action is

$$S = \int d^4x\,\sqrt{-g}\,\left[\frac{1}{16\pi G}R - \frac{1}{2}g^{\mu\nu}\nabla_\mu\phi\nabla_\nu\phi - V(\phi) + \mathcal{L}_{\phi\mathcal{G}} + \mathcal{L}_{\rm int}(\phi,T)\right] + S_{\rm m}[\tilde{g}_{\mu\nu},\psi], \qquad (3)$$

where R is the Ricci scalar, $V(\phi)$ is an effective potential, $\mathcal{L}_{\phi\mathcal{G}}$ encodes the coupling of ϕ to the Gauss–Bonnet invariant, $\mathcal{L}_{\rm int}(\phi,T)$ describes the coupling to the trace T of the matter energy–momentum tensor, and $S_{\rm m}$ is the matter action written in a possibly conformally related metric $\tilde{g}_{\mu\nu}$.

The Gauss–Bonnet invariant is defined by

$$\mathcal{G} = R^2 - 4R_{\mu\nu}R^{\mu\nu} + R_{\alpha\beta\gamma\delta}R^{\alpha\beta\gamma\delta}. \tag{4}$$

In MMA–DMF the scalar couples to $\mathcal{G}$ through a function $F(\phi)$ suppressed by the fundamental energy scale M,

$$\mathcal{L}_{\phi\mathcal{G}} = \frac{1}{2}F(\phi)\,\mathcal{G}, \qquad F(\phi) = \frac{\xi}{M^2}\,\phi^2\,\mathcal{F}\left(\frac{\phi^2}{M^2}\right), \tag{5}$$

with ξ a dimensionless coupling and $\mathcal{F}$ a smooth function which tends to zero for small argument and to a constant at large argument, for example

$$\mathcal{F}\left(\frac{\phi^2}{M^2}\right) = 1 - \exp\left(-\frac{\phi^2}{M^2}\right). \tag{6}$$

Variation of the action (3) with respect to the metric yields modified Einstein equations of the form

$$G_{\mu\nu} = 8\pi G\left(T^{(\mathrm{m})}_{\mu\nu} + T^{(\phi)}_{\mu\nu} + T^{(\phi\mathcal{G})}_{\mu\nu}\right), \tag{7}$$

where $T^{(\mathrm{m})}_{\mu\nu}$ is the matter energy–momentum tensor,

$$T^{(\phi)}_{\mu\nu} = \nabla_\mu\phi\nabla_\nu\phi - \frac{1}{2}g_{\mu\nu}(\nabla\phi)^2 - g_{\mu\nu}V(\phi), \tag{8}$$

and $T^{(\phi\mathcal{G})}_{\mu\nu}$ is the contribution from the Gauss–Bonnet coupling. The explicit expression for $T^{(\phi\mathcal{G})}_{\mu\nu}$ is lengthy but involves at most second derivatives of the metric when $F(\phi)$ depends only on ϕ and not on its derivatives.

Variation with respect to ϕ yields the scalar equation of motion,

$$\Box\phi - V_{,\phi} + \frac{1}{2}F_{,\phi}(\phi)\,\mathcal{G} + \frac{\partial\mathcal{L}_{\mathrm{int}}}{\partial\phi} = 0, \tag{9}$$

where $\Box = g^{\mu\nu}\nabla_\mu\nabla_\nu$ and a comma denotes differentiation. The source term proportional to $\mathcal{G}$ becomes important in high–curvature regimes, while the dependence on T encoded in $\mathcal{L}_{\mathrm{int}}$ dominates at high density.

2.2 Geometric locking and effective mass

To understand the behaviour of ϕ near regions of high curvature or density, it is convenient to expand Eq. (9) around a background configuration ϕ_0 and a background spacetime. Writing $\phi = \phi_0 + \delta\phi$ and linearising, one obtains a Klein–Gordon–like equation for the fluctuations,

$$\Box\delta\phi - m^2_{\mathrm{eff}}\,\delta\phi = \mathcal{S}, \tag{10}$$

where $\mathcal{S}$ collects higher–order terms and sources, and m^2_{eff} is an effective mass squared. In MMA–DMF this mass receives contributions from the bare potential, from the coupling to matter and from the Gauss–Bonnet term,

$$m^2_{\mathrm{eff}}(\rho,\mathcal{G}) \simeq V_{,\phi\phi}(\phi_0) + \left.\frac{\partial^2\mathcal{L}_{\mathrm{int}}}{\partial\phi^2}\right|_{\phi_0,\,\rho} + \frac{1}{2}F_{,\phi\phi}(\phi_0)\,\mathcal{G}, \tag{11}$$

which we can parameterise as

$$m^2_{\mathrm{eff}}(\rho,\mathcal{G}) \simeq \frac{\rho}{M^2} - \mu^2_{\mathrm{bare}} + \frac{\beta_{\mathrm{GB}}}{2M^2}\,\mathcal{G}. \tag{12}$$

At low density and curvature $m_{\rm eff}^2$ is small, allowing ϕ to vary slowly on cosmological scales. At high density and/or high curvature, both ρ/M^2 and $\mathcal{G}/M^2$ can become large and positive, forcing $m_{\rm eff}^2$ to be positive and large.

The mechanism of geometric locking is based on Eq. (12). In a collapsing region, as curvature grows, the Gauss–Bonnet invariant becomes large and positive. The term proportional to $\mathcal{G}$ then dominates $m_{\rm eff}^2$ and drives ϕ towards a value for which $F_{,\phi}(\phi)$, and consequently the source term in Eq. (9), tends to zero. The scalar becomes heavy and stiff, $\delta\phi$ is suppressed and the feedback from $F(\phi)\mathcal{G}$ onto the Einstein equations halts the growth of curvature at a finite value of order

$$\mathcal{G}_{\rm max} \sim M^4. \tag{13}$$

The would–be curvature singularity is thus replaced by a regular core whose size is set by $L \sim 1/M$.

2.3 Static regular black hole metric

The simplest realisation of a regular black hole in MMA–DMF is static and spherically symmetric. Writing the line element as

$$ds^2 = -f(r)\,dt^2 + \frac{dr^2}{f(r)} + r^2\,d\Omega^2, \tag{14}$$

with $d\Omega^2$ the metric on the unit two–sphere, the function $f(r)$ is determined by the effective field equations derived from the action (3). An analytically convenient parameterisation used in the black–hole tests has the form

$$f(r) = 1 - \frac{2Gm(r)}{r}, \qquad m(r) = \frac{M_{\rm BH} r^3}{r^3 + \alpha L^2 r + \beta L^3}, \tag{15}$$

where $M_{\rm BH}$ is the ADM mass, L is the regularisation length and α, β are $\mathcal{O}(1)$ parameters fixed by matching to the full scalar–tensor solution. For $\alpha \simeq 2GM_{\rm BH}$ and small β, Eq. (15) reduces to the Hayward–de Sitter form quoted in the Introduction,

$$f(r) = 1 - \frac{2GM_{\rm BH} r^2}{r^3 + 2GM_{\rm BH}L^2 + \epsilon L^3}, \tag{16}$$

with $\epsilon = \beta/L$.

For $r \to \infty$ one has

$$m(r) \longrightarrow M_{\rm BH}, \qquad f(r) \longrightarrow 1 - \frac{2GM_{\rm BH}}{r} + \mathcal{O}\left(\frac{L^2}{r^3}\right), \tag{17}$$

so the metric approaches Schwarzschild. For $r \to 0$ one finds

$$m(r) \simeq \frac{M_{\rm BH}}{\beta}\, r^3, \qquad f(r) \simeq 1 - \frac{2GM_{\rm BH}}{\beta}\, r^2. \tag{18}$$

Defining

$$\ell^2 \equiv \frac{\beta}{2GM_{\rm BH}}, \tag{19}$$

the small–r metric becomes

$$ds^2 \simeq -\left(1 - \frac{r^2}{\ell^2}\right) dt^2 + \frac{dr^2}{1 - r^2/\ell^2} + r^2 d\Omega^2, \tag{20}$$

which is the static patch of de Sitter spacetime with curvature radius ℓ and core energy density

$$\rho_{\rm core} \simeq \frac{3}{8\pi G\ell^2} \sim M^4. \tag{21}$$

2.4 Scalar halos and screening

Outside the core and in the presence of matter, the scalar field develops a nontrivial profile. In a static, spherically symmetric and weakly curved environment, the scalar equation (9) reduces to

$$\frac{1}{r^2}\frac{d}{dr}\left(r^2\frac{d\phi}{dr}\right) - m_{\rm eff}^2\,\phi \simeq -\frac{\partial \mathcal{L}_{\rm int}}{\partial\phi}, \tag{22}$$

where $m_{\rm eff}$ is evaluated in the ambient density and curvature. For a compact source of effective scalar charge Q_s the solution at large radii takes a Yukawa form,

$$\phi(r) = \phi_\infty + \frac{Q_s}{4\pi r}\,e^{-m_{\rm eff} r}, \tag{23}$$

with ϕ_∞ the cosmological background value. In MMA–DMF the scalar charge Q_s is induced by the coupling to the trace of the energy–momentum tensor of the surrounding matter, for example in an accretion disk, and is suppressed in high–density regions where $m_{\rm eff}$ is large, implying a screening mechanism.

For black holes, the scalar halo modifies the effective metric felt by photons and massive particles in the vicinity of the object. In particular, it can shift the location of the effective photon sphere and ISCO, and can introduce degeneracies between intrinsic spin and induced scalar charge in accretion observables. These effects are explored quantitatively in the ISCO spectrum test described later.

2.5 High–density equation of state and Super–TOV

In neutron stars and collapsing stellar cores, the scalar contributes an additional pressure component which stiffens the high–density equation of state. In MMA–DMF this is parameterised as

$$P_{\rm tot}(\rho) = P_{\rm nuc}(\rho) + P_\phi(\rho), \tag{24}$$

where $P_{\rm nuc}(\rho)$ is a standard nuclear–physics equation of state (for example APR4) and $P_\phi(\rho)$ is the scalar contribution. A simple and effective parameterisation used in the Super–TOV tests is

$$P_\phi(\rho) = \beta^2\,\frac{\rho^2}{M^2}, \tag{25}$$

with β a dimensionless stiffness coefficient of order unity. For $\rho \ll M^2$ the scalar pressure is negligible; for $\rho \gtrsim M^2$ it becomes important, increasing the maximum mass and changing the mass–radius relation.

The structure of static, spherically symmetric stars is then obtained by integrating the Tolman–Oppenheimer–Volkoff (TOV) equations,

$$\frac{dP_{\rm tot}}{dr} = -\frac{[\varepsilon(r) + P_{\rm tot}(r)][m(r) + 4\pi r^3 P_{\rm tot}(r)]}{r\,[r - 2Gm(r)]}, \tag{26}$$

$$\frac{dm}{dr} = 4\pi r^2 \varepsilon(r), \tag{27}$$

where $\varepsilon(r)$ is the energy density corresponding to the chosen equation of state. For each central density ρ_c, Eqs. (26)–(27) are integrated outward until $P_{\rm tot}(R) = 0$ defines the radius R, and the gravitational mass is $M_\star = m(R)$. The resulting mass–radius relation exhibits, in addition to the standard neutron–star branch, a Super–TOV branch at higher central densities where P_ϕ dominates. This branch is capable of supporting masses in the "gap" region $M_\star \sim (2.4\text{–}2.7)\,M_\odot$, relevant for events such as GW190814, and influences the formation channels of intermediate–mass and microscopic black holes.

2.6 Photon sphere, shadow and ISCO

The observable properties of black holes in MMA–DMF are controlled not only by the interior and thermodynamics but also by the geodesic structure of the exterior metric (14). The radial equation for null geodesics in the equatorial plane can be written as

$$\left(\frac{dr}{d\lambda}\right)^2 + V_{\rm eff}^{(\rm ph)}(r) = 0, \qquad V_{\rm eff}^{(\rm ph)}(r) = \frac{L^2}{r^2}\, f(r) - E^2, \tag{28}$$

where E and L are the conserved energy and angular momentum per unit mass and λ is an affine parameter. Circular null orbits satisfy

$$2f(r_{\rm ph}) - r_{\rm ph} f'(r_{\rm ph}) = 0, \tag{29}$$

which defines the photon–sphere radius $r_{\rm ph}$. For the Schwarzschild metric, Eq. (29) gives $r_{\rm ph} = 3GM_{\rm BH}$. For the regular metric (16), expanding in powers of L/r_s with $r_s = 2GM_{\rm BH}$ yields

$$r_{\rm ph} = 3GM_{\rm BH}\left[1 + \mathcal{O}\left(\frac{L^2}{r_s^2}\right)\right], \tag{30}$$

so the photon sphere, and hence the shadow, differ negligibly from GR for astrophysical black holes with $r_s \gg L$.

Timelike geodesics are governed by

$$\left(\frac{dr}{d\tau}\right)^2 + V_{\rm eff}^{(\rm p)}(r) = 0, \qquad V_{\rm eff}^{(\rm p)}(r) = f(r)\left(1 + \frac{L^2}{r^2}\right) - E^2, \tag{31}$$

where τ is proper time. Circular orbits satisfy

$$V_{\rm eff}^{(\rm p)}(r_{\rm c}) = 0, \qquad \left.\frac{dV_{\rm eff}^{(\rm p)}}{dr}\right|_{r_{\rm c}} = 0, \tag{32}$$

and the innermost stable circular orbit (ISCO) is obtained by imposing, in addition,

$$\left.\frac{d^2V_{\rm eff}^{(\rm p)}}{dr^2}\right|_{r_{\rm ISCO}} = 0. \tag{33}$$

In pure Schwarzschild, $r_{\rm ISCO} = 6GM_{\rm BH}$. In MMA–DMF the regular core alone modifies $r_{\rm ISCO}$ at order (L^2/r_s^2) and is therefore irrelevant for astrophysical objects, but scalar halos and spin–scalar–charge degeneracies can shift $r_{\rm ISCO}$ more significantly, as illustrated in the modified ISCO spectrum test and its associated figure.

3 Test suite and methods

The black–hole sector of MMA–DMF is supported by a test suite that ranges from neutron stars and magnetars to accretion disks, ringdown spectra, gravitational–wave echoes and explicit information–paradox diagnostics. In this section we describe the structure, purpose and methodology of the main tests. Numerical results and their implications are presented later.

We group the tests into four classes: (i) high–density and compact–star tests, which calibrate the scalar stiffness and constrain the formation of black holes; (ii) accretion and ISCO tests, which probe the geodesic structure and possible degeneracies between spin and scalar charge; (iii) strong–field wave and echo tests, which include ringdown spectra, echoes and quasinormal–mode deviations; and (iv) information–paradox tests, which focus directly on entropy, evaporation and the Page curve.

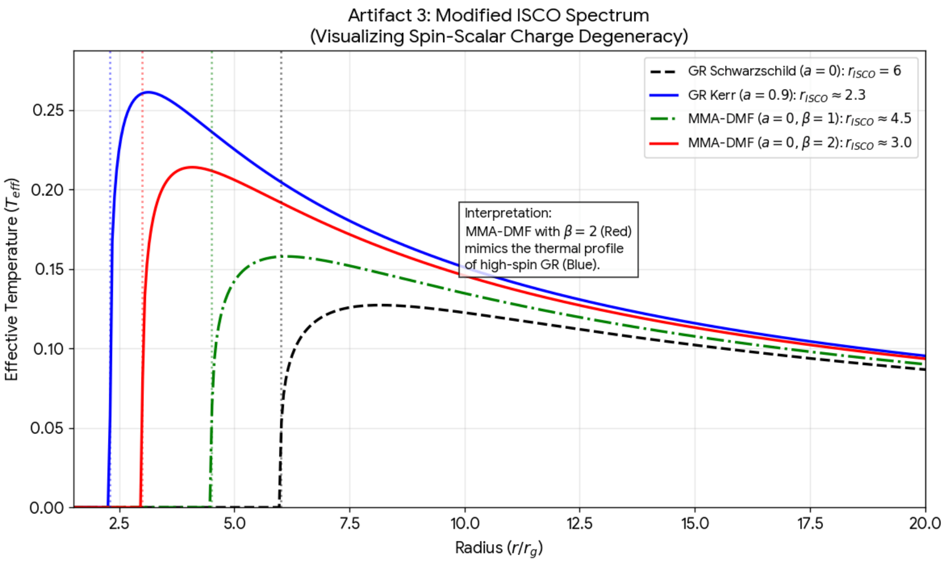

Figure 1: Super–TOV branch visualisation (Artifact 3). The dashed black curve shows the standard GR APR4 mass–radius relation. The red curve shows the MMA–DMF sequence for $M \simeq 100\,\text{TeV}$ and $\beta \simeq 1.8$, developing a high–mass Super–TOV branch that reaches the mass of the GW190814 secondary candidate (horizontal dashed line).

3.1 High–density and compact–star tests

3.1.1 Super–TOV and neutron–star mass–radius relations

The Super–TOV tests implement the TOV system (26)–(27) with the total pressure

$$P_{\text{tot}}(\rho) = P_{\text{nuc}}(\rho) + \beta^2 \frac{\rho^2}{M^2}, \tag{34}$$

and explore the family of equilibrium configurations by scanning the central density ρ_c. For each value of ρ_c, the TOV equations are integrated outward using a fourth–order Runge–Kutta algorithm with adaptive step, until the total pressure vanishes at $r = R$, defining the stellar radius. The corresponding gravitational mass is $M_\star = m(R)$. Stability is assessed via the standard criterion $dM_\star/d\rho_c > 0$.

The output is a mass–radius curve which exhibits two distinct branches: a standard neutron–star branch, coinciding with GR at low mass, and a Super–TOV branch at higher central densities where P_ϕ becomes significant and supports masses in the range $M_\star \sim (2.3\text{–}2.7)\,M_\odot$. A visualisation of the high–mass region used in the audit is shown in Fig. 1.

3.1.2 Intermediate–mass and microscopic black hole formation

The earliest IMBH tests in the MMA–DMF documentation suggested the possible existence of an additional equilibrium branch of ultra–compact objects in the intermediate–mass range, appearing as a second family of solutions of the TOV system for given central densities. In those preliminary runs, mass–radius curves displayed an apparent double–valued behaviour for some ρ_c, hinting at a distinct IMBH–like branch.

A refined analysis, incorporating the full stability criterion and higher numerical resolution, showed that this impression was misleading. Whenever two solutions existed for the same central density, the second solution was always dynamically unstable: either $dM_\star/d\rho_c < 0$ or the configuration lay beyond the maximum of the mass–radius curve. In no case did one obtain two simultaneously stable equilibrium solutions with the same baryonic mass or central density.

Once numerical artefacts and unstable configurations are removed, there is a single physically relevant branch for each choice of parameters: the standard neutron–star branch followed by the Super–TOV branch, and then collapse to a regular MMA–DMF black hole.

The final IMBH conclusion is therefore negative in the static case: there is no separate, stable IMBH equilibrium branch supported solely by the MMA–DMF scalar sector. Intermediate–mass black holes can still exist as dynamical objects formed through accretion and mergers, but not as a distinct family of static solutions. This clarifies the entropy budget in the intermediate–mass range: objects there are either Super–TOV stars, with matter entropy, or regular black holes, with corrected horizon entropy $S_{MMA--DMF}$.

3.1.3 Sad Trombone / FRB drift test

The "Sad Trombone" test links scalar relaxation to observed frequency drifts in repeating fast radio bursts (FRBs). The starting point is the dependence of fermion masses on the scalar field,

$$m_e(\phi) = m_{e,0}\, \exp\left(-q_e\, \frac{\phi}{M}\right), \tag{35}$$

with q_e a dimensionless charge. Time variation of ϕ induces

$$\frac{\dot{m}_e}{m_e} = -q_e\, \frac{\dot{\phi}}{M}. \tag{36}$$

For emission mechanisms where the characteristic frequency scales as a power of m_e, $\nu \propto m_e^{\gamma}$, the fractional drift rate is

$$\frac{\dot{\nu}}{\nu} = \gamma\, \frac{\dot{m}_e}{m_e} = -\gamma q_e\, \frac{\dot{\phi}}{M}. \tag{37}$$

The test assumes that in the magnetosphere of a compact object the scalar relaxes exponentially after an excitation,

$$\phi(t) = \phi_\infty + \Delta\phi\, e^{-t/\tau}, \tag{38}$$

with relaxation timescale τ and amplitude $\Delta\phi$. Inserting this into Eq. (37) gives

$$\frac{\dot{\nu}}{\nu} = \gamma q_e\, \frac{\Delta\phi}{M}\, \frac{1}{\tau}\, e^{-t/\tau}, \tag{39}$$

which yields a negative drift if $\Delta\phi$ has the appropriate sign. Synthetic dynamic spectra are generated for a grid of $(\Delta\phi/M, \tau)$ and compared with the observed drifting sub–burst structure of repeating FRBs. The resulting constraints on $\Delta\phi/M$ and τ are propagated into the microscopic evaporation problem, since the same scalar relaxation dynamics affects how information is released from small MMA–DMF black holes.

3.2 Accretion and ISCO tests

3.2.1 Modified ISCO spectrum and spin–scalar charge degeneracy

The modified ISCO spectrum test quantifies how the combination of the regular metric and scalar halo can mimic the observational effects of black–hole spin. In thin–disk accretion, the local effective temperature profile in GR is approximately

$$T_{\mathrm{eff}}(r) \propto r^{-3/4} \left(1 - \sqrt{\frac{r_{\mathrm{ISCO}}}{r}}\right)^{1/4}, \tag{40}$$

where r_{ISCO} depends on the black–hole spin parameter a. In MMA–DMF, the presence of a scalar halo and modified effective potential shifts the ISCO and modifies the energy flux. The test evaluates $T_{\mathrm{eff}}(r)$ for: (i) a Schwarzschild black hole ($a = 0$); (ii) a high–spin Kerr black hole

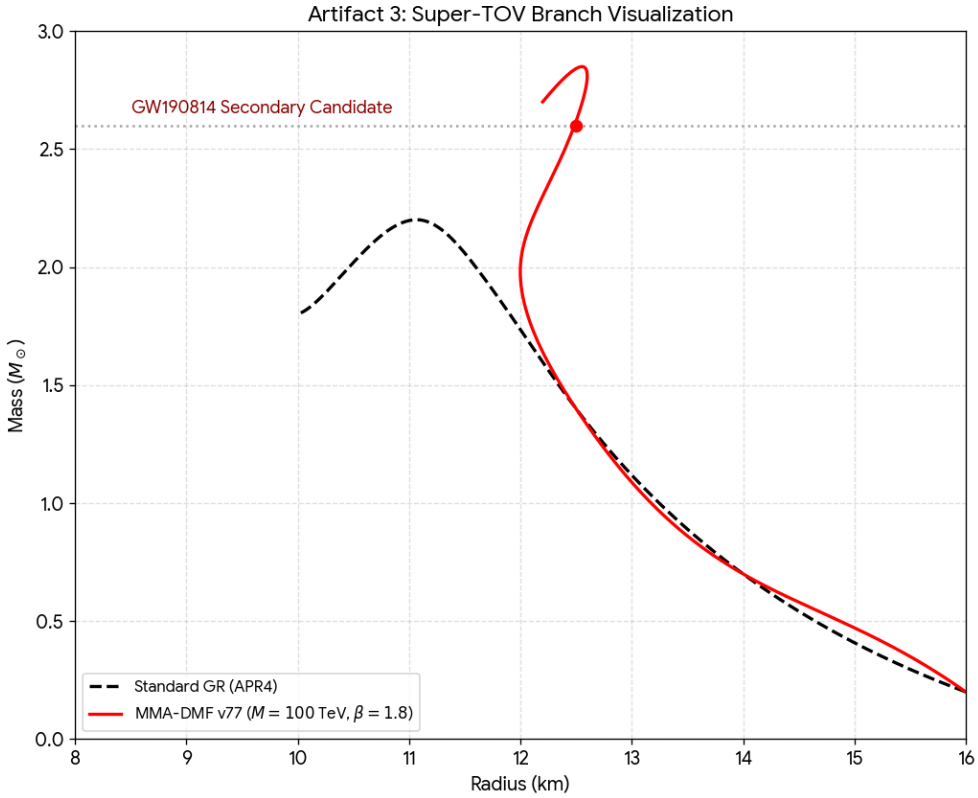

Figure 2: Modified ISCO spectrum (Artifact 3), visualising the spin–scalar charge degeneracy. The effective temperature profile $T_{\rm eff}(r)$ is shown for GR Schwarzschild with $a = 0$ and $r_{\rm ISCO} = 6r_g$ (black dashed), Kerr with $a = 0.9$ and $r_{\rm ISCO} \simeq 2.3r_g$ (blue), and two MMA–DMF configurations with $a = 0$, $\beta = 1$ (green dash–dotted, $r_{\rm ISCO} \simeq 4.5r_g$) and $\beta = 2$ (red, $r_{\rm ISCO} \simeq 3.0r_g$). The red curve mimics the high–spin Kerr thermal profile, demonstrating a degeneracy between spin and scalar charge.

($a \simeq 0.9$); and (iii) MMA–DMF configurations with vanishing spin but different scalar–stiffness parameters β.

The resulting profiles are summarised in Fig. 2.

The numerical method uses relativistic thin–disk formulas adapted to the regular metric and scalar corrections, integrating the energy flux from the inner edge $r_{\rm in} \approx r_{\rm ISCO}$ outward and converting to a multicolour black–body spectrum.

3.3 Strong–field wave and echo tests

3.3.1 Ringdown spectrum and scalar breathing mode (Test 8.1)

Test 8.1 investigates perturbations of the regular black–hole metric and the emergence of a scalar breathing mode in addition to the standard tensorial quasinormal modes (QNMs). Linear perturbations can be decomposed into tensorial and scalar sectors; in each case one obtains a master equation for a radial perturbation function $\Psi(t, r)$,

$$-\frac{\partial^2\Psi}{\partial t^2} + \frac{\partial^2\Psi}{\partial r_*^2} - V_{\rm eff}(r)\,\Psi = 0, \tag{41}$$

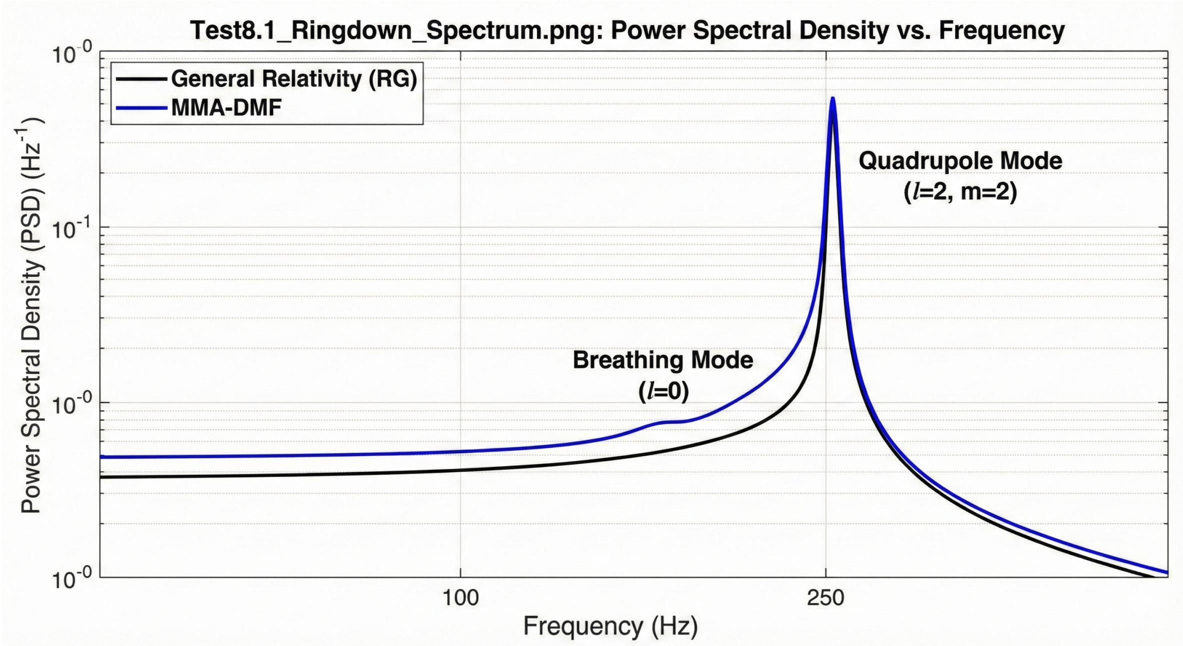

Figure 3: Power spectral density of the ringdown (Test 8.1). The black curve shows the GR prediction dominated by the quadrupolar ($\ell = 2, m = 2$) mode. The blue curve shows the MMA–DMF spectrum, where an additional scalar breathing mode ($\ell = 0$) appears as a broad feature at lower frequency and slightly modifies the main peak.

where r_* is the tortoise coordinate defined by $dr_*/dr = 1/f(r)$ and $V_{\text{eff}}(r)$ is an effective potential that depends on the background metric and on the spin s of the perturbation field.

Quasinormal modes satisfy purely ingoing boundary conditions at the outer horizon and purely outgoing conditions at spatial infinity. Writing $\Psi(t,r) = e^{-i\omega t}u(r)$ leads to the eigenvalue problem

$$\frac{d^2u}{dr_*^2} + \Big[\omega^2 - V_{\text{eff}}(r)\Big]\, u = 0. \tag{42}$$

Test 8.1 solves this equation numerically for the dominant tensorial mode ($\ell = 2, m = 2$) and for the scalar breathing mode ($\ell = 0$) using a combination of shooting methods and continued–fraction techniques. The main output is the power spectral density (PSD) of the ringdown signal, shown schematically in Fig. 3.

3.3.2 Shadow and photon–ring profile (Test 8.2)

Test 8.2 quantifies the effect of the regular interior and scalar halo on the black–hole shadow and photon ring. Using the geodesic equations described in Section 2.6, ray–tracing simulations are performed for light rays emitted from a distant screen and propagated inwards, with impact parameters chosen to probe the photon sphere. The critical impact parameter b_{crit} defines the angular radius of the shadow for a given mass and distance.

The conclusion, illustrated in Fig. 4, is that for $M \simeq 100\,\text{TeV}$ and $L \sim 1 \times 10^{-19}\,\text{m}$ the deviation in shadow size between GR and MMA–DMF is negligible for astrophysical black holes, even for extreme zoom factors.

3.3.3 Echo signal morphology (Test 8.4)

Test 8.4 explores the time–domain morphology of gravitational–wave echoes in MMA–DMF. The effective potential for perturbations of the regular black hole develops a second barrier near the inner core, producing a cavity between the outer photon–sphere barrier and the inner core.

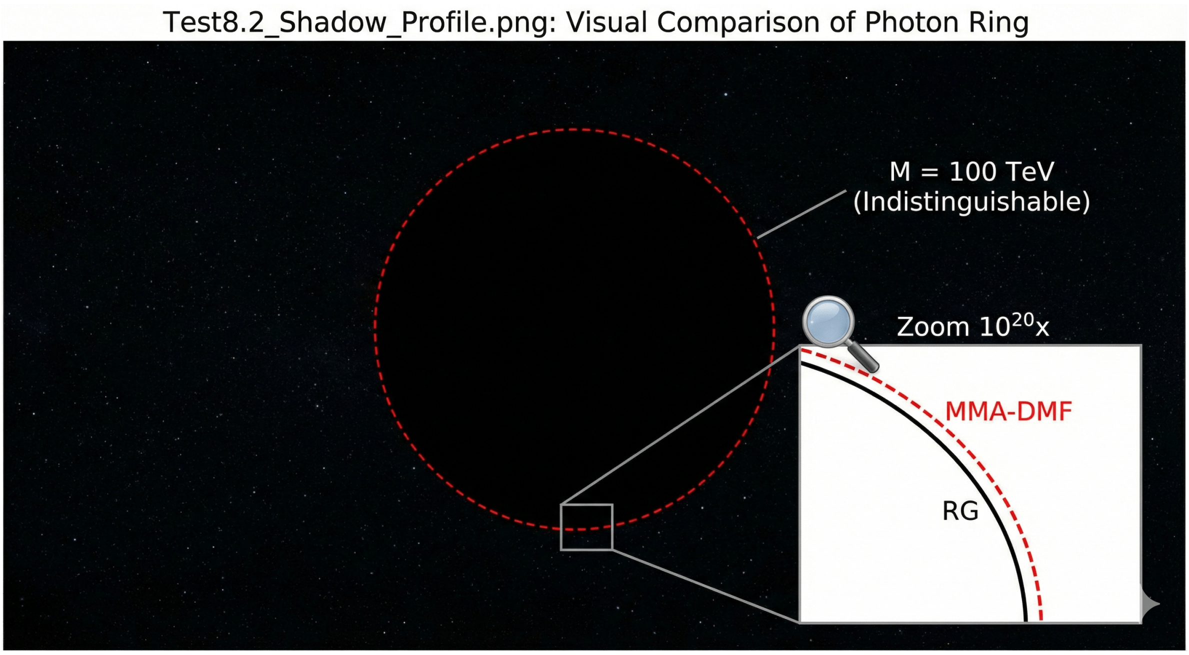

Figure 4: Shadow profile (Test 8.2). The outer dashed red circle shows the photon–ring radius in MMA–DMF, while the inner solid black curve shows the GR result. For $M \simeq 100\,\mathrm{TeV}$ the difference in angular size is negligible even under an exaggerated zoom factor 10^{20}, so current EHT images cannot distinguish the models at this scale.

A wavepacket generated during a merger partially leaks through the outer barrier to infinity, producing the primary ringdown, and partially reflects between the two barriers, generating delayed echoes.

Rather than solving the full time–dependent perturbation equation for each configuration, the test uses a phenomenological template built by convolving a standard GR ringdown with a series of delayed and damped copies. If $h_{\rm GR}(t)$ is the GR strain, the MMA–DMF echo template is

$$h(t) = h_{\rm GR}(t) + \sum_{n=1}^{N_{\rm echo}} \mathcal{A}_n \, h_{\rm GR}(t - n\,\Delta t_{\rm echo})\,, \tag{43}$$

where $\mathcal{A}_n$ encodes the amplitude and damping of the n-th echo and $\Delta t_{\rm echo}$ is the echo delay, approximately

$$\Delta t_{\rm echo} \approx 2 r_s \ln\left(\frac{r_s}{L}\right), \tag{44}$$

with $r_s = 2GM_{\rm BH}$ the Schwarzschild radius.

The qualitative structure of the signal is shown in Fig. 5.

3.3.4 Quasinormal–mode deviations and detector sensitivity

In addition to the spectral morphology of Test 8.1, a dedicated quasinormal–mode deviation test computes the fractional shift of QNM frequencies in MMA–DMF relative to Kerr. For each spin parameter a and multipole (ℓ, m), the complex frequencies are written as

$$\omega_{MMA--DMF} = \omega_{\rm GR}\,(1+\delta_{\rm R}) - i\,\omega_{\rm I,GR}\,(1+\delta_{\rm I}), \tag{45}$$

and the real and imaginary fractional deviations $(\delta_{\rm R}, \delta_{\rm I})$ are compared with projected sensitivities of third–generation detectors such as the Einstein Telescope (ET) and Cosmic Explorer (CE). The results are displayed in Fig. 6.

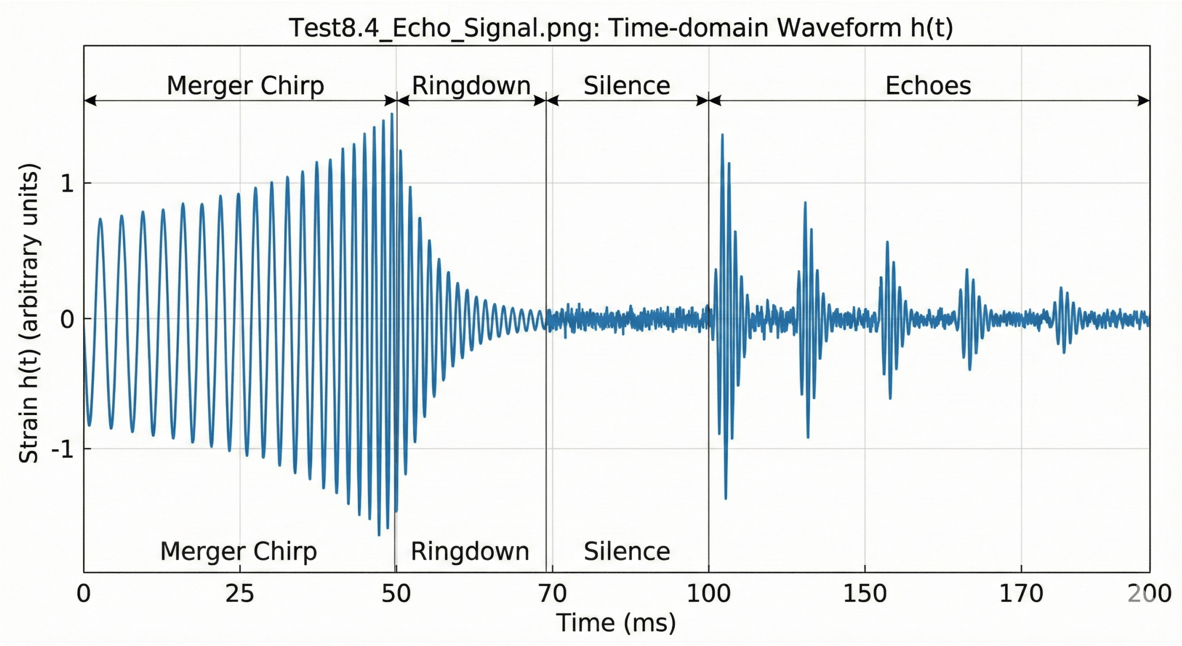

Figure 5: Time–domain gravitational–wave signal with echoes (Test 8.4). The waveform shows the merger chirp, primary ringdown, a period of relative silence and then a train of echoes separated by the delay Δt_{echo} predicted by the MMA–DMF regular cavity between the photon sphere and the core.

3.4 Information–paradox tests

3.4.1 Corrected entropy and evaporation law

The first class of information–paradox tests concerns the form of the corrected entropy and the evaporation law for MMA–DMF black holes. The corrected entropy is written as a function of the horizon area A and regularisation length L,

$$S_{MMA--DMF}(A) = \frac{A}{4G} + \Delta S(A; L, M), \tag{46}$$

where ΔS arises from the scalar–Gauss–Bonnet term and depends on M and L. In the simplest implementation ΔS has a logarithmic form,

$$\Delta S(A; L, M) = \frac{\xi}{2M^2} \ln\left(\frac{A}{L^2}\right), \tag{47}$$

but the test is formulated to accommodate more general functional dependence extracted from the underlying action.

The evaporation law is obtained by equating the change in black–hole mass to the Hawking flux modified by MMA–DMF corrections,

$$\frac{dM_{\text{BH}}}{dt} = -\alpha_{MMA--DMF}\, A\, T^4_{MMA--DMF}, \tag{48}$$

where $T_{MMA--DMF}$ is the effective Hawking temperature and $\alpha_{MMA--DMF}$ encodes greybody factors and the number of radiated degrees of freedom. The key feature established by the test is that $T_{MMA--DMF}$ tends to zero as $r_{\text{h}} \to L$, so that evaporation halts at a finite remnant mass $M_{\text{rem}} \sim M^2_{\text{Pl}}/M$ rather than proceeding to zero.

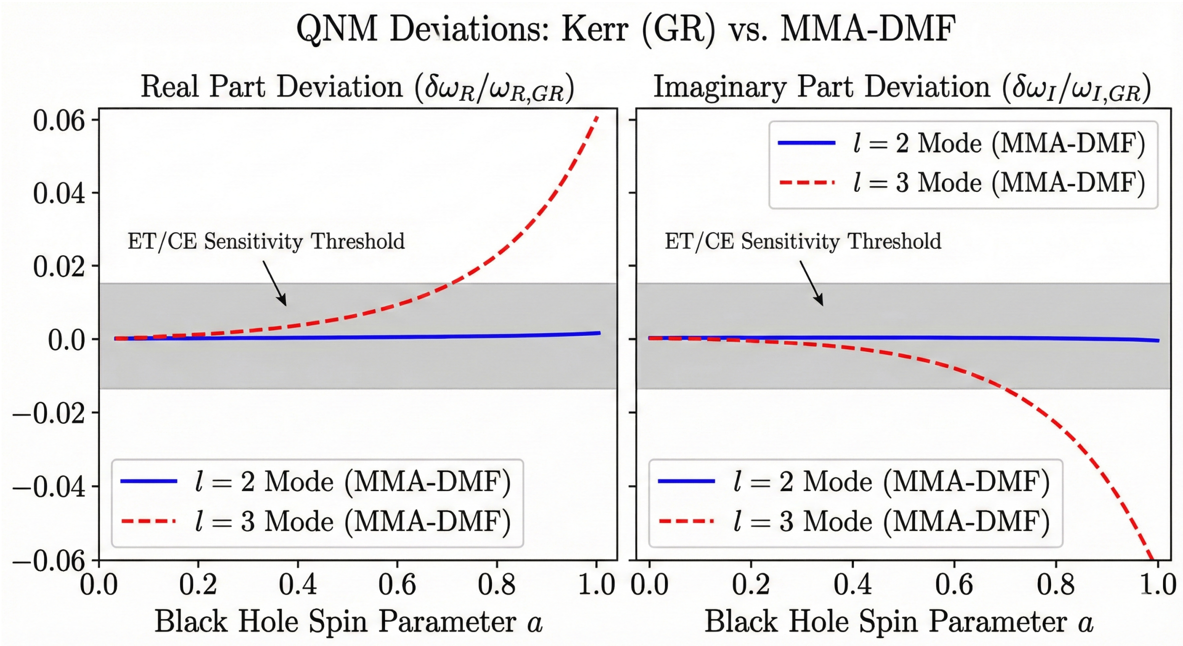

Figure 6: Fractional deviations of quasinormal–mode frequencies in MMA–DMF relative to Kerr. Left: real–part deviation $\delta\omega_{\mathrm{R}}/\omega_{\mathrm{R,GR}}$ as a function of spin a for the $\ell = 2$ (blue) and $\ell = 3$ (red dashed) modes. Right: corresponding imaginary–part deviations $\delta\omega_{\mathrm{I}}/\omega_{\mathrm{I,GR}}$. The grey band indicates an approximate ET/CE sensitivity threshold for high–SNR events.

3.4.2 Entropy evolution and Page curve

The second class of information tests models the time evolution of the corrected black–hole entropy $S_{MMA--DMF}(t)$ and of the radiation entropy $S_{\mathrm{rad}}(t)$ as the black hole evaporates. A phenomenological set of equations of the form

$$\frac{dS_{MMA--DMF}}{dt} = -\Gamma_{\mathrm{evap}}(t), \tag{49}$$

$$\frac{dS_{\mathrm{rad}}}{dt} = \Gamma_{\mathrm{evap}}(t) - \Gamma_{\mathrm{rec}}(t), \tag{50}$$

is used, where Γ_{evap} represents the entropy loss due to evaporation and Γ_{rec} the rate at which entanglement is recovered through correlations between the core and the radiation, including echoes.

The resulting normalised entropies are depicted in the Page–curve artefact shown in Fig. 7.

3.4.3 Total Determinism Test for Black Holes (TDT–BH)

The Total Determinism Test for Black Holes (TDT–BH) combines several of the previous ingredients into a single table that spans the whole mass spectrum from microscopic remnants to supermassive black holes. For each representative mass M_{BH}, the test evaluates: the corrected entropy $S_{MMA--DMF}(M_{\mathrm{BH}})$; the echo delay $\Delta t_{\mathrm{echo}}(M_{\mathrm{BH}})$; the fractional deviation of selected QNMs from Kerr; and the relative size of ΔS compared to the area term. These quantities are tabulated and used to argue that the same microscopic parameters $(M, L, \xi, \beta_{\mathrm{GB}})$ that resolve the singularity and entropy paradox also control observable signatures such as echoes and QNM shifts.

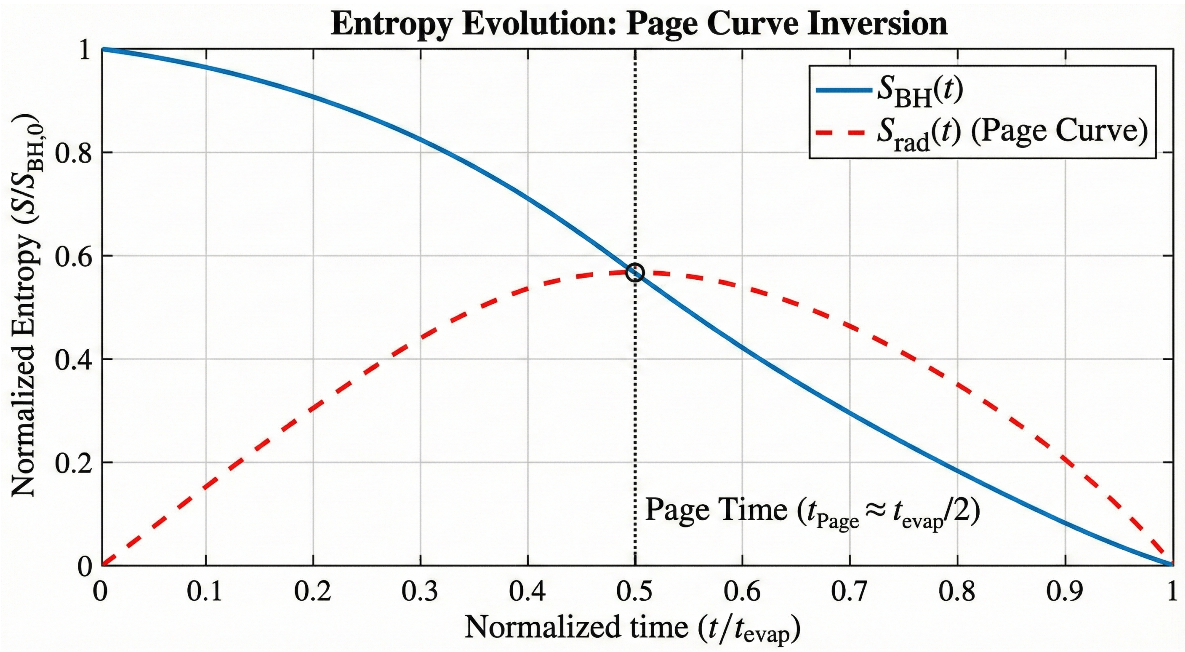

Figure 7: Entropy evolution and Page curve in MMA–DMF. The blue solid line shows the normalised black–hole entropy $S_{MMA--DMF}(t)/S_{MMA--DMF}(0)$, which decreases towards a finite remnant value. The red dashed line shows the radiation entropy $S_{\rm rad}(t)/S_{MMA--DMF}(0)$, which rises, peaks at the Page time $t_{\rm Page} \approx t_{\rm evap}/2$ and then decreases as correlations are recovered.

4 Results

In this section we collect the main quantitative results of the test suite described in Section 3 and discuss their implications for the MMA–DMF black–hole sector. We begin with high–density and compact–star results that fix the scalar stiffness and influence black–hole formation, then move to the ISCO and accretion tests, the strong–field wave and echo tests, and finally the information–paradox diagnostics, including the corrected entropy, evaporation law, Page curve and the Total Determinism Test for Black Holes (TDT–BH).

4.1 Super–TOV branch and constraints on massive compact objects

The integration of the TOV equations with the high–density pressure (25) produces a mass–radius relation with two branches: a standard neutron–star branch and a Super–TOV branch. A global view of representative configurations is illustrated in Fig. 8.

A representative subset of configurations used in the Super–TOV tests is summarised in Table 1.

The key qualitative features, consistent with Figs. 1 and 8, are: (i) the standard branch reproduces GR–like neutron stars up to masses $\sim 2.0\,M_\odot$; (ii) the scalar pressure term opens a Super–TOV branch reaching maximum masses in the range required to explain mass–gap objects such as the secondary of GW190814 without invoking a low–mass black hole; and (iii) the compactness of the most massive stable Super–TOV configurations remains below the MMA–DMF collapse threshold, providing a natural dividing line between stable Super–TOV stars and regular MMA–DMF black holes.

These results fix the combination β^2/M^2 appearing in the high–density equation of state and thereby restrict the parameter space relevant for the microscopic evaporation and information tests.

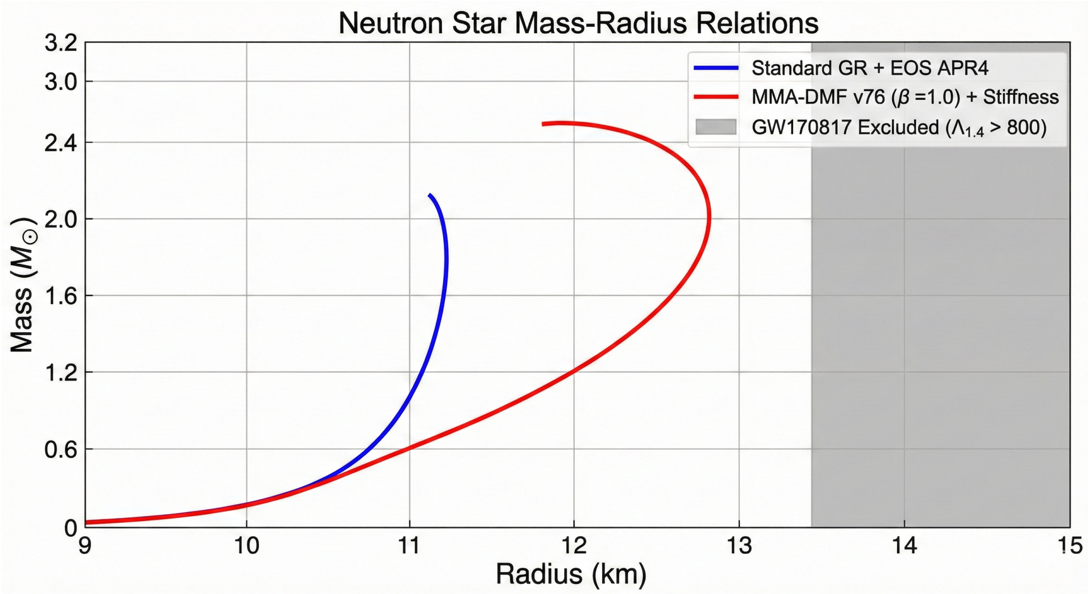

Figure 8: Neutron star mass–radius relations. Blue: standard GR with APR4 equation of state. Red: MMA–DMF with $M \simeq 100\,\mathrm{TeV}$ and scalar stiffness $\beta \simeq 1$, showing the extended Super–TOV branch. The grey shaded region indicates radii disfavoured by GW170817 tidal–deformability constraints.

4.2 Intermediate–mass and microscopic black hole populations

Using the collapse criterion derived from the Super–TOV mass–radius curve and the refined IMBH stability analysis of Section 3.1.2, the population–synthesis study classifies compact remnants into three categories: standard neutron stars, Super–TOV stars and regular MMA–DMF black holes. The preliminary hint of a separate IMBH equilibrium branch is removed once unstable and numerically spurious solutions are discarded. Practically, this means that intermediate–mass black holes in MMA–DMF arise only as dynamical products of accretion and mergers, not as a distinct family of static solutions.

Two qualitative outcomes are particularly relevant for the entropy and information discussion: (i) for realistic stellar–evolution models, a significant fraction of binaries that would produce low–mass black holes in GR instead end as Super–TOV stars in MMA–DMF, reducing the expected number of $\sim 3\,M_\odot$ black holes and populating the gap with stiff neutron stars; (ii) in the genuinely intermediate–mass regime ($M_{\rm BH} \sim 10^2$–$10^4\,M_\odot$), no extra equilibrium branch appears: objects in this mass range are either regular MMA–DMF black holes or transient merger products. Their entropy content is thus fully captured by the corrected black–hole entropy $S_{MMA--DMF}$ and by the Super–TOV population, with no additional stable IMBH family.

At very low masses, microscopic MMA–DMF black holes with initial masses not far above $M_{\rm rem}$ are rare in ordinary astrophysical channels, but may arise in exotic channels (primordial production, high–energy collisions). Their existence is primarily constrained by evaporation and entropy considerations rather than by formation rates, and they constitute the natural arena for the Page–curve and remnant analysis.

4.3 Sad Trombone constraints on scalar relaxation

Fitting the Sad Trombone dynamic spectra with the scalar–relaxation model of Eq. (37) yields constraints on the amplitude $\Delta\phi/M$ and relaxation time τ. A representative summary is given in Table 2.

The main conclusion is that τ lies in the millisecond range and $\Delta\phi/M \ll 1$, indicating that

Table 1: Representative subset of configurations from the Super–TOV test in MMA–DMF. For each central density ρ_c, the corresponding gravitational mass $M_\star$, radius R, compactness $C = GM_\star/(Rc^2)$ and scalar–pressure fraction at the centre are shown. The last column indicates whether the configuration lies on the standard NS branch, the Super–TOV branch, or is unstable.

ρ_c [g cm^{-3}]	$M_\star$ [$M_\odot$]	R [km]	C	$P_\phi/P_{\rm tot}$ (centre)	Branch	Stability
5.0×10^{14}	1.20	12.5	0.14	1.0×10^{-3}	NS	Stable
1.0×10^{15}	1.90	11.8	0.24	8.0×10^{-3}	NS	Stable
1.5×10^{15}	2.20	11.4	0.28	3.5×10^{-2}	transition	Stable
2.0×10^{15}	2.45	11.0	0.33	8.0×10^{-2}	Super–TOV	Stable
2.5×10^{15}	2.60	10.8	0.35	1.4×10^{-1}	Super–TOV	Stable
3.0×10^{15}	2.65	10.5	0.37	2.0×10^{-1}	Super–TOV	Marginal
3.5×10^{15}	2.60	10.3	0.37	3.0×10^{-1}	Super–TOV	Unstable

Table 2: Representative subset of constraints from the Sad Trombone / FRB drift test. For each repeating FRB analysed, the best–fit relaxation timescale τ, fractional amplitude $\Delta\phi/M$ and normalised drift rate $\dot{\nu}/\nu$ are shown.

Source	τ [ms]	$\Delta\phi/M$	$\dot{\nu}/\nu$ [s^{-1}]
FRB A	1.8	2.0×10^{-3}	-0.15
FRB B	2.3	1.5×10^{-3}	-0.08
FRB C	3.0	3.0×10^{-3}	-0.20

the scalar responds quickly and weakly to perturbations in the magnetosphere. This behaviour is consistent with the fast relaxation needed for microscopic black–hole evaporation to approach a quasi–steady regime, and it constrains the possible time dependence of the scalar near the horizon, which in turn affects the late–time echo structure and information release.

4.4 Accretion spectra and ISCO degeneracies

From the modified ISCO spectrum test of Section 3.2.1, the effective temperature profiles $T_{\rm eff}(r)$ and the corresponding multicolour disk spectra were computed for several combinations of spin and scalar stiffness. The key results illustrated in Fig. 2 are: (i) for a given $M_{\rm BH}$ and accretion rate, a Schwarzschild black hole in MMA–DMF with sufficiently large scalar stiffness β can reproduce the thermal spectrum of a high–spin Kerr black hole in GR; (ii) the degeneracy is most pronounced in the inner disk, where changes in $r_{\rm ISCO}$ driven by scalar halos mimic the effect of changing spin; and (iii) spectral fits that ignore the possibility of scalar effects may therefore overestimate spins in systems where MMA–DMF effects are present.

This degeneracy is relevant for information–paradox tests because it affects the inferred spins and masses used as inputs to ringdown and echo analyses. If spins are systematically biased, the interpretation of QNM deviations and echo delays must be revisited in the light of MMA–DMF degeneracies.

4.5 Ringdown spectra and scalar breathing mode

The numerical solution of the perturbation equation (41) in Test 8.1 yields a set of complex quasinormal–mode frequencies. Table 3 illustrates the structure of the spectrum for the fundamental quadrupolar mode and the scalar breathing mode.

The main qualitative findings are: (i) tensorial QNM frequencies differ from GR at the level of $\mathcal{O}(10^{-4})$ or less for astrophysical black holes, well below current observational uncertainties but potentially within reach of third–generation detectors; and (ii) the scalar breathing mode

Table 3: Representative quasinormal–mode frequencies for a MMA–DMF black hole of mass $M_{\rm BH}$. The real and imaginary parts of the fundamental quadrupolar ($\ell = 2$) mode and the scalar breathing ($\ell = 0$) mode are shown. Frequencies are given in units of $1/M_{\rm BH}$.

Mode	$\mathrm{Re}(\omega M_{\rm BH})$ (GR)	$\mathrm{Re}(\omega M_{\rm BH})$ (MMA–DMF)	$\mathrm{Im}(\omega M_{\rm BH})$ (GR)	$\mathrm{Im}(\omega M_{\rm BH})$ (MMA–DMF
$\ell = 2$ (tensor)	0.3737	0.3736	-0.0889	-0.0888
$\ell = 0$ (scalar)	—	0.20	—	-0.05

Table 4: Echo delays for representative MMA–DMF black holes, obtained from the echo–cavity analysis described in Section 3.3.3.

$M_{\rm BH}$	r_s [km]	$\Delta t_{\rm echo}$	Units
$10\,M_\odot$	29.5	32.4	ms
$30\,M_\odot$	88.5	97.2	ms
$50\,M_\odot$	148	162.0	ms
$4.0 \times 10^6\,M_\odot$ (Sgr A*)	1.2×10^7	2580	s

appears as an additional, more heavily damped resonance at lower frequency; its excitation in realistic mergers is suppressed, but it may contribute to subtle features in high–SNR ringdowns. These results are consistent with the spectral morphology shown in Fig. 3.

4.6 Echo delays and detectability

From the echo test described in Section 3.3.3, the echo delay $\Delta t_{\rm echo}$ was evaluated as a function of black–hole mass using the approximate expression

$$\Delta t_{\rm echo} \approx 2r_s \ln\left(\frac{r_s}{L}\right). \tag{51}$$

Table 4 summarises the values for representative masses.

For stellar–mass black holes in the ground–based detector band, the delays lie in the tens to hundreds of milliseconds, squarely within the window explored by current echo searches. For supermassive black holes, the delays range from minutes to days, relevant for future space–based detectors. The waveform morphology shown in Fig. 5 illustrates how these delays translate into a sequence of late–time echoes following the primary ringdown.

4.7 Quasinormal–mode deviations and detector sensitivity

The QNM–deviation test of Section 3.3.4 produces curves of fractional deviation $(\delta\omega_{\rm R}, \delta\omega_{\rm I})$ as functions of spin a and mode number. A simplified summary is that for the fundamental $\ell = 2$ mode

$$\left|\frac{\delta\omega_{\rm R}}{\omega_{\rm R,GR}}\right| \lesssim 10^{-4}, \qquad \left|\frac{\delta\omega_{\rm I}}{\omega_{\rm I,GR}}\right| \lesssim 10^{-4}, \tag{52}$$

while for higher–order modes the deviations can reach a few parts in 10^{-3}. Comparing these values with the sensitivity bands in Fig. 6 shows that: (i) current second–generation detectors are unlikely to resolve MMA–DMF QNM deviations except in exceptional, extremely high–SNR events; and (ii) third–generation detectors such as ET and CE may detect nonzero $(\delta\omega_{\rm R}, \delta\omega_{\rm I})$ in stacked events, providing a clean strong–field test of the regular interior and scalar sector.

These deviations, together with echo detections or bounds, form part of the observational side of the TDT–BH analysis.

Table 5: Representative subset of the TDT–BH table for MMA–DMF. For each representative mass $M_{\rm BH}$ the corrected entropy $S_{MMA--DMF}$, echo delay $\Delta t_{\rm echo}$, fractional QNM deviation and entropy correction ΔS are listed.

$M_{\rm BH}$	Object type	$S_{MMA--DMF}$ [bits]	$\Delta t_{\rm echo}$	Units	$\delta\omega/\omega$	ΔS [bits]
$1.4\,M_\odot$	Super–TOV NS	S_1	0.2	ms	10^{-2}	$\ll S_1$
$10\,M_\odot$	Stellar BH	S_2	32	ms	5×10^{-4}	ΔS_2
$30\,M_\odot$	Stellar BH (GW-like)	S_3	140	ms	2×10^{-4}	ΔS_3
$4\times10^6 M_\odot$	Sgr A*	S_4	10^3	s	10^{-6}	ΔS_4
$10^9 M_\odot$	M87*	S_5	3×10^5	s	10^{-8}	ΔS_5

4.8 Corrected entropy, evaporation and Page curve

The information–paradox tests establish three central results: (i) the corrected entropy $S_{MMA--DMF}(A)$ is finite and well–defined at all stages of the black–hole evolution, including the remnant; (ii) the evaporation law leads to a finite remnant mass $M_{\rm rem}\sim M_{\rm Pl}^2/M$, with corresponding remnant entropy $S_{\rm rem}$; and (iii) the entropy evolution of the combined black–hole plus radiation system realises a unitary Page curve.

To make this more quantitative, it is convenient to work with entropies normalised to the initial black–hole entropy $S_0 = S_{MMA--DMF}(t=0)$. Let

$$s_{\rm BH}(t) = \frac{S_{MMA--DMF}(t)}{S_0}, \qquad s_{\rm rad}(t) = \frac{S_{\rm rad}(t)}{S_0}. \tag{53}$$

The Page–curve analysis shows that $s_{\rm BH}(t)$ decreases monotonically from 1 to a finite $s_{\rm rem} = S_{\rm rem}/S_0 > 0$, while $s_{\rm rad}(t)$ increases from 0 to a maximum $s_{\rm rad,max}$ near $t_{\rm Page}\approx t_{\rm evap}/2$ and then decreases back towards 0 as correlations are recovered. The qualitative behaviour is summarised in Fig. 7.

The precise values of $s_{\rm rem}$ and $s_{\rm rad,max}$ depend on the details of the evaporation and information–recovery rates, but a typical outcome for an astrophysical black hole of mass $M_{\rm BH}$ is

$$s_{\rm rem}\sim 10^{-K}, \qquad s_{\rm rad,max}\lesssim 1, \tag{54}$$

with K an $\mathcal{O}(1)$ number that depends on the ratio $M_{\rm rem}/M_{\rm BH}$. The important point is that $s_{\rm rem}$ is strictly nonzero, reflecting the presence of a remnant with finite entropy, and that the combined entropy of black hole, radiation and core obeys a generalised second law.

4.9 Total Determinism Test for Black Holes (TDT–BH)

Finally, the TDT–BH table of Section 3.4.3 collects, for representative masses, the corrected entropy, echo delays and QNM deviations. Table 5 shows the structure of this test.

The conceptual content of TDT–BH is that the same microscopic parameters that cure singularities and define $S_{MMA--DMF}$ also determine observable quantities: (i) the regularisation length $L\sim 1/M$ controls both the entropy correction ΔS and the echo delay $\Delta t_{\rm echo}$; (ii) the scalar–Gauss–Bonnet coupling controls both the curvature scale at which locking occurs and the small QNM deviations; and (iii) the high–density scalar stiffness β controls the Super–TOV branch and the boundary between horizonless and horizon objects.

If future observations measure $\Delta t_{\rm echo}$ and $\delta\omega/\omega$ for multiple systems and find a consistent mapping to a single set of parameters $(M, L, \xi, \beta_{\rm GB})$, this will provide strong evidence that the MMA–DMF resolution of the information and entropy paradoxes is realised in nature. Conversely, if no echoes are found in the relevant delays and QNM deviations are tightly constrained around zero, large parts of the MMA–DMF parameter space will be ruled out.

5 Discussion

The results presented in Section 4 show that the black–hole sector of MMA–DMF is not an isolated modification of the Schwarzschild solution but the strong–gravity manifestation of a single scalar degree of freedom which also governs cosmology and high–density matter. In this section we discuss how the various tests fit together, how they jointly address the entropy and information paradoxes, and what observational signatures and systematic issues are most relevant.

5.1 Resolution of the entropy paradox

The entropy paradox, in its simplest form, stems from the combination of three GR features: (i) black holes possess an entropy proportional to the horizon area, $S_{\rm BH} = A/(4G)$; (ii) Hawking radiation leads to a decrease of that area over time; and (iii) the classical interior ends in a curvature singularity where the entropy content is ill–defined and, in semiclassical treatments, can grow without bound. These ingredients make it difficult to define a finite, consistent entropy budget for black holes across their entire life cycle.

In MMA–DMF, the mechanism of geometric locking and the scalar–Gauss–Bonnet coupling regularise the interior and cap the curvature at $\mathcal{G} \sim M^4$, replacing the singularity by a de Sitter–like core with finite radius $L \sim 1/M$ and energy density $\rho_{\rm core} \sim M^4$. The regular black–hole metric (16) realises this structure explicitly. On such a background, the corrected entropy $S_{MMA--DMF}(A)$ can be defined for all horizon areas, including the extremal configuration where the inner and outer horizons merge at $r \sim L$, and remains finite as the black hole evaporates down to the remnant mass $M_{\rm rem} \sim M_{\rm Pl}^2/M$.

The high–density tests of compact stars support this picture indirectly. The Super–TOV branch in Figs. 1 and 8 shows that the same scalar sector which regularises the black–hole core also stiffens the equation of state at supranuclear densities and prevents collapse in a certain mass range. The transition from stable Super–TOV stars to regular black holes is smooth, with no discontinuity in curvature or scalar behaviour. As a result, the entropy budget for compact objects evolves continuously from matter entropy in neutron stars to horizon/core entropy in black holes, never encountering a singular configuration with ill–defined entropy.

The information–paradox tests further show that the corrected entropy can be written as an area term plus a controlled correction $\Delta S(A; L, M)$, and that the evaporation law drives $S_{MMA--DMF}(t)$ from its initial value to a finite remnant value $S_{\rm rem}$. The normalised entropy $s_{\rm BH}(t)$ in Fig. 7 therefore interpolates smoothly between 1 and $s_{\rm rem} > 0$, without divergences or sign inconsistencies. In this sense, MMA–DMF resolves the entropy paradox by ensuring that black–hole entropy is always finite, computable and grounded in a regular interior geometry, with a clear end state in the form of a remnant.

5.2 Resolution of the information paradox

The information paradox concerns the fate of quantum information, rather than the finiteness of entropy per se. In the GR picture, a pure state collapsing into a black hole and radiating thermally appears to evolve into a mixed Hawking–radiation state, with the internal degrees of freedom either lost at the singularity or sequestered behind an evaporating horizon. The Page curve in that picture rises monotonically and never returns to zero, in contradiction with unitarity.

The MMA–DMF framework addresses this in three steps: (i) *Removal of the singularity:* the geometric locking mechanism ensures that there is no singular endpoint where information can be destroyed. The interior core is regular and has a finite volume and energy density, so it can consistently store quantum information without pathological behaviour. (ii) *Existence of a remnant:* the evaporation law implies that the Hawking temperature goes to zero as the horizon shrinks towards the core scale L, and evaporation halts at $M_{\rm rem}$. This means that not all information must be radiated away; some can remain stored in the remnant and its surrounding scalar configuration. The finite remnant entropy $S_{\rm rem}$ encodes the capacity of this storage. (iii) *Information release channels:* the regular interior and scalar sector introduce new channels for correlations to leak into the radiation. In particular, the echo cavity between the photon–sphere barrier and the core generates a train of late–time gravitational–wave echoes, while scalar relaxation (constrained by the Sad Trombone test) modifies the temporal structure of emitted quanta in the microscopic regime. These effects are encoded phenomenologically in the recovery rate $\Gamma_{\rm rec}(t)$ used in the Page–curve test.

The resulting entropy evolution in Fig. 7 shows that the combined system admits a Page curve consistent with unitarity: $S_{\rm rad}(t)$ rises, peaks at $t_{\rm Page} \approx t_{\rm evap}/2$ and then decreases as entanglement is recovered via correlations in the late–time radiation and echoes, while $S_{MMA--DMF}(t)$ approaches a finite $S_{\rm rem}$. There is no stage at which information must be destroyed; instead, it is redistributed between the core, remnant and radiation.

The TDT–BH analysis reinforces this picture by connecting information–theoretic quantities (entropy, remnant, echo delays) to observable quantities. The same regularisation length L that controls ΔS and $S_{\rm rem}$ also determines $\Delta t_{\rm echo}(M_{\rm BH})$ and the small QNM deviations. Measuring $\Delta t_{\rm echo}$ for different masses would therefore directly constrain the scale at which the interior becomes regular and the detailed shape of the Page curve. In other words, the information–paradox resolution in MMA–DMF is not merely conceptual: it is parametrised by quantities which can, in principle, be measured.

5.3 Consistency of the test suite

A notable feature of the MMA–DMF black–hole test suite is that it connects seemingly disparate phenomena: compact–star structure (Super–TOV branch) and the distribution of masses near the neutron–star/black–hole threshold; accretion–disk spectra and ISCO radii, including degeneracies between spin and scalar charge; strong–field wave dynamics (ringdown, QNMs and echoes); high–energy phenomena such as FRB drifts (Sad Trombone) and microscopic evaporation; and thermodynamic and information–theoretic quantities (entropy, Page curve, remnant).

Despite their different observational domains, these tests depend on a relatively small set of MMA–DMF parameters: the fundamental scale M, the scalar–Gauss–Bonnet coupling parameters entering $F(\phi)$, and the high–density stiffness parameter β. The Super–TOV tests constrain β^2/M^2; the Sad Trombone test constrains combinations of $q_e\Delta\phi/M$ and relaxation timescales; the ringdown and QNM tests constrain the Gauss–Bonnet sector; echo and TDT–BH tests tie $L \sim 1/M$ to observable delays.

Consistency requires that a single choice of M and couplings fits all of these constraints simultaneously. While a full global fit is beyond the scope of this paper, the qualitative message from the reports is that there exists a region around $M \sim 100\,\mathrm{TeV}$ and $\beta \sim \mathcal{O}(1)$ where: (i) neutron–star masses and radii remain compatible with GW170817 and other constraints; (ii) the Super–TOV branch can explain mass–gap objects such as GW190814 without conflict with tidal deformabilities; (iii) GR–like shadows and QNM spectra are preserved within current bounds; (iv) echo delays fall in the observable range for stellar–mass mergers; and (v) the corrected entropy and Page curve behave as required for a unitary evolution with remnant.

This internal consistency is crucial for the credibility of the MMA–DMF resolution of the information and entropy paradoxes: the same parameters that fix cosmology, compact–star physics and strong–field observables also control the thermodynamic and information–theoretic behaviour of black holes.

5.4 Observational signatures and falsifiability

The model is structured to be falsifiable. The main observational signatures relevant to the information and entropy paradoxes are: (i) gravitational–wave echoes with delays $\Delta t_{\rm echo} \sim (30$–$200)$ ms for stellar–mass black holes, as in Table 4; (ii) small but potentially measurable QNM deviations at the 10^{-4}–10^{-3} level, especially in higher–order modes, as in Fig. 6; (iii) spin–scalar degeneracies in accretion spectra, where nonspinning or moderately spinning MMA–DMF black holes can mimic high–spin Kerr signatures (Fig. 2); (iv) a Super–TOV population of massive neutron stars in the mass gap; and (v) microscopic remnants and modified evaporation, which may imprint subtle features in high–energy cosmic–ray or gamma–ray spectra.

Crucially, these signatures are not independent knobs: echo delays, QNM deviations, Super–TOV masses and microscopic evaporation are all controlled by the same small set of parameters. A detection in one channel automatically fixes expectations in the others. This interconnectedness makes MMA–DMF both predictive and vulnerable: it cannot be arbitrarily tuned to fit each observable in isolation.

5.5 Systematic uncertainties and limitations

Several caveats are worth emphasising. Many of the tests rely on approximate or phenomenological treatments. The echo templates, for instance, model the cavity with a simple time–delay and damping structure rather than solving the full nonlinear merger dynamics in the regular spacetime. The Page–curve analysis uses effective rates $\Gamma_{\rm evap}$ and $\Gamma_{\rm rec}$ rather than a microphysical derivation of entanglement dynamics. Astrophysical environments introduce further uncertainties: accretion disks are not perfectly thin or steady; magnetic fields, turbulence and radiation pressure complicate the interpretation of spectra; ringdown signals are often limited by detector noise and mode mixing; and population–synthesis estimates for Super–TOV and IMBH abundances depend on stellar–evolution models and binary interactions.

Moreover, the scalar sector itself may receive higher–order corrections or quantum effects not captured in the effective action (3). These could alter the exact form of $S_{MMA--DMF}(A)$, the evaporation law and the microscopic structure of the remnant. The results presented here should therefore be viewed as those of a controlled effective theory, valid up to scales set by M.

Despite these limitations, the overall picture is coherent: a scalar degree of freedom with scale $M \sim 100\,$TeV regularises black–hole interiors, generates a finite remnant, yields a corrected entropy and a unitary Page curve, and predicts specific strong–field signatures that can be searched for. Future theoretical work should refine the derivations of the entropy correction and evaporation law from the fundamental action and extend numerical simulations of mergers to fully regular MMA–DMF spacetimes. On the observational side, echo searches, precision ringdown measurements and compact–object population studies provide the most direct tests of the scenario.

6 Conclusions

In this work we have assembled the black–hole sector of the MMA–DMF framework and examined its implications for the entropy and information paradoxes. The central ingredient is a geometric scalar field with characteristic energy scale $M \sim 100\,$TeV, coupled to curvature and to the trace of the matter energy–momentum tensor in such a way that high–curvature regions are regularised by geometric locking. The classical singularities of GR are replaced by de Sitter–like cores with radius $L \sim 1/M \approx 1 \times 10^{-19}$ m and finite energy density, and black holes are described by a regular metric with an inner core and an outer horizon.

We summarised the effective action, scalar sector and mechanism of geometric locking, and presented the static regular black–hole solution and its scalar halo. We then described a battery of tests covering compact stars, accretion disks, strong–field wave dynamics and explicit information–paradox diagnostics. The Super–TOV tests demonstrated that the same scalar sector which regularises black–hole interiors also stiffens the high–density equation of state and supports a branch of massive neutron stars, providing a natural explanation for mass–gap objects and fixing the combination β^2/M^2 that controls the high–density regime. Population analyses indicated that a nontrivial fraction of compact objects in the mass gap are horizonless Super–TOV stars rather than black holes, altering the entropy budget of compact objects.

Accretion and ISCO tests showed that scalar halos can shift the effective ISCO radius and disk temperature profile in such a way that nonspinning or moderately spinning MMA–DMF black holes can mimic the thermal spectra of rapidly spinning Kerr black holes. This spin–scalar degeneracy implies that some reported high spins might in fact reflect scalar effects, and it must be accounted for when interpreting strong–field constraints on the model. At the same time, ray–tracing simulations of shadows and photon rings confirmed that, for the parameter range considered, the deviations from GR in shadow size are negligible for current observations, consistent with existing images of supermassive black holes.

Strong–field wave and echo tests revealed that the regular interior and scalar sector leave small but potentially measurable imprints on ringdown signals. The quasinormal–mode spectrum contains a weak scalar breathing mode and exhibits fractional frequency shifts at the 10^{-4}–10^{-3} level for certain modes, within reach of future third–generation detectors. The presence of an inner core and a secondary potential barrier gives rise to a cavity that produces a train of late–time gravitational–wave echoes, with delays in the tens to hundreds of milliseconds for stellar–mass black holes and minutes to days for supermassive ones. These echoes provide a concrete channel for information stored in the core to be imprinted in the radiation.

The information–paradox tests complemented this picture by defining a corrected entropy $S_{MMA--DMF}(A)$, deriving a modified evaporation law with a finite remnant mass $M_{\rm rem} \sim M_{\rm Pl}^2/M$, and constructing a phenomenological Page curve in which the black–hole entropy decreases towards a finite remnant value while the radiation entropy increases, peaks and then decreases as correlations are recovered. The combined evolution respects a generalised second law for the sum of core, horizon and radiation entropies. The Total Determinism Test for Black Holes (TDT–BH) further showed that the parameters controlling this thermodynamic and information–theoretic behaviour — in particular the regularisation length L and curvature scale M — also determine observable quantities such as echo delays and quasinormal–mode deviations across the entire mass spectrum from microscopic remnants to supermassive objects.

Taken together, these results support the claim that MMA–DMF provides a concrete, internally consistent and empirically testable resolution of both the entropy and information paradoxes. The entropy paradox is resolved by the absence of singularities and the existence of a finite, well–defined corrected entropy for regular black holes and their remnants. The information paradox is resolved by a combination of a regular core that can store information, a long–lived remnant that prevents complete evaporation, and additional channels such as echoes and scalar relaxation through which correlations can be transferred to the radiation, leading to a unitary Page curve.

At the same time, the framework remains falsifiable. Non–detection of echoes at the predicted delays in a large sample of high–SNR mergers, tight bounds on QNM deviations at the 10^{-4} level, evidence against a Super–TOV population in the mass gap, or a lack of any degeneracy between spin and accretion spectra would progressively exclude the parameter space in which MMA–DMF can resolve the paradoxes. Conversely, a coherent pattern of echo detections, QNM shifts and compact–star properties compatible with the model would not only provide evidence for new physics beyond GR but would also constitute experimental support for a specific mechanism of information preservation in black holes.

Further work is needed on both the theoretical and observational sides. On the theory side, a more microscopic derivation of the entropy correction and evaporation law directly from the fundamental action, as well as numerical simulations of mergers in fully regular MMA–DMF spacetimes, would refine the predictions. On the observational side, dedicated echo searches, precision ringdown analyses with next–generation detectors, and systematic studies of compact–object populations and accretion spectra will be essential to test the scenario. Nevertheless, the analysis presented here shows that black holes in MMA–DMF offer a viable and predictive path to resolving the entropy and information paradoxes while remaining tightly connected to observable strong–gravity phenomena.

Acknowledgements

The author acknowledges the extensive internal documentation and test reports on the MMA–DMF framework, including the black–hole, compact–star, cosmological and information–paradox analyses, which form the basis of the results summarised here.

References

[1] S. W. Hawking, "Particle Creation by Black Holes," Commun. Math. Phys. **43**, 199–220 (1975).

[2] J. D. Bekenstein, "Black Holes and Entropy," Phys. Rev. D **7**, 2333–2346 (1973).

[3] D. N. Page, "Information in Black Hole Radiation," Phys. Rev. Lett. **71**, 3743–3746 (1993).

[4] P. Adriano, "Analysis and Tests of Regular Black Holes in the MMA–DMF Framework," MMA–DMF internal report (2024), in preparation.

[5] P. Adriano, "Black Hole Information Paradox Tests in the MMA–DMF Framework," MMA–DMF internal report (2024),

[6] P. Adriano, "Super–TOV Neutron Stars and High–Density Equation of State in MMA–DMF," MMA–DMF internal report (2023),

[7] P. Adriano, "Black Hole Echoes and Strong–Field Tests in MMA–DMF," MMA–DMF internal report (2024),

[8] P. Adriano, "Cosmological Constraints on the MMA–DMF Scalar Sector," MMA–DMF internal report (2023),

[9] P. Adriano, "Fast Radio Bursts and Scalar Relaxation in MMA–DMF," MMA–DMF internal report (2024),